

Article

Optimization of the Operating Voltage of Cobalt-Free Nickel-in-Medium Cathodes for High-Performance Lithium-Ion Batteries

Yuchuan Qi ¹, Shuheng Hou ², Ningbo Qin ¹, Ting Huang ¹, Jiawen Guo ³, Xianghua Hou ^{3,*}, Ning Huang ¹, Yifan Liu ^{4,*} and Xijun Liu ^{1,*} 

¹ Guangxi Institute of Science and Technology Development, Nanning 530022, China; qiyuchuan112@163.com (Y.Q.); qnb2012@163.com (N.Q.); huangt0108@163.com (T.H.); gxkjjjkfzx@163.com (N.H.)

² Mathematics & Physics, Guangxi University Nationalities, Nanning 530006, China; m18269102958@163.com

³ Institute of New Functional Materials, Guangxi Institute of Industrial Technology, Nanning 530200, China; 15177779218@163.com

⁴ Institute of Advanced Science Facilities, Shenzhen 518107, China

* Correspondence: 2314402016@st.gxu.edu.cn (X.H.); liuyf@mail.iasf.ac.cn (Y.L.); liuxjtjut@163.com (X.L.)

Abstract: Medium-nickel cobalt-free cathode materials have attracted much attention in recent years for their low cost and high energy density. However, the structural stability of nickel-based cathode materials becomes compromised when accompanied by the increasing of voltage, leading to poor cycling performance and, thus, hindering their widespread industrial application. In this work, we investigated the optimal charge cut-off voltage for the nickel-based cathode material $\text{LiNi}_{0.6}\text{Mn}_{0.4}\text{O}_2$ (NM64). Within the voltage range of 3.0 to 4.5 V, the electrode energy density reached 784.08 Wh/kg, with an initial Coulombic efficiency of 84.49%. The reversible specific capacity at 0.1 C reached 197.84 mAh/g, and it still maintained a high reversible specific capacity of nearly 150 mAh/g, with a capacity retention rate of 86% after 150 cycles at 1 C. Furthermore, NM64 exhibited an intact morphological structure without noticeable cracking after 150 cycles, indicating excellent structural stability. This study emphasizes the relationship between the stability of NM64 cathodes and different operating voltage ranges, thereby promoting the development of high-voltage layered nickel-based cathode materials.

Keywords: cobalt-free cathode; charge cut-off voltage; reversible specific capacity; cycle stability; lithium-ion battery



Citation: Qi, Y.; Hou, S.; Qin, N.; Huang, T.; Guo, J.; Hou, X.; Huang, N.; Liu, Y.; Liu, X. Optimization of the Operating Voltage of Cobalt-Free Nickel-in-Medium Cathodes for High-Performance Lithium-Ion Batteries. *Batteries* **2024**, *10*, 273. <https://doi.org/10.3390/batteries10080273>

Academic Editor: Diana Golodnitsky

Received: 4 July 2024

Revised: 21 July 2024

Accepted: 25 July 2024

Published: 30 July 2024



Copyright: © 2024 by the authors. Licensee MDPI, Basel, Switzerland. This article is an open access article distributed under the terms and conditions of the Creative Commons Attribution (CC BY) license (<https://creativecommons.org/licenses/by/4.0/>).

1. Introduction

As the automotive industry transitions to electrification, rechargeable lithium-ion batteries (LIBs) are gradually becoming the cornerstone for meeting high-energy density requirements. Currently, significant progress has been made in various aspects of improving battery performance, while the high cost of raw materials remains a persistent obstacle [1,2]. Cobalt (Co) is an important material component of commercial cathodes [3,4], for example, LiCoO_2 , $\text{LiNi}_x\text{Co}_y\text{Mn}_{1-x-y}\text{O}_2$, and $\text{LiNi}_x\text{Co}_y\text{Al}_{1-x-y}\text{O}_2$. However, due to various global supply chain issues, recent raw material prices have continued to rise, especially cobalt sources. Even more importantly, the rarity of cobalt ore is due to its low abundance and uneven distribution in the earth's crust, so its use faces significant cost limitations. The limited availability of cobalt resources will result in the traditional high-nickel NCM ($\text{LiNi}_x\text{Co}_y\text{Mn}_{1-x-y}\text{O}_2$) cathode materials being economically unviable as a predominant strategy in the electric vehicle market [5,6]. Indeed, reducing the cost of batteries and minimizing their dependence on the external environment is currently the most optimal strategy [7–9]. To achieve this goal, researchers have focused on high-nickel (Ni), low- or

no-cobalt layered cathode materials, which have greatly promoted the development of cobalt-free laminated cathode materials [10].

For cobalt-free cathode materials, Yu et al. [11] reported cobalt-free NM90 with an optimized growth of 010 crystal planes by a Zr doping discharge capacity of more than 220 mAh/g at 0.1 C under a cut-off voltage of 4.3 V. Michael et al. [12] reported LiNO₂ by an Mg-doped B-coated discharge capacity of more than 242 mAh/g at 0.1 C under a cut-off voltage of 4.3 V. High capacity and energy density can be achieved with a Ni-rich layered oxide cathode [13]. However, it is clear that substituting cobalt with nickel directly (e.g., LiNiO₂) is not a viable option. The decreased thermal stability of the material structure results in a notable decline in battery performance [14]. Therefore, employing inexpensive metals to replace a portion of the cobalt in the cathode structure is an effective approach to maintain material stability and battery performance [15]. Recently, medium-nickel cathode materials such as NCM-523 and NCM-622 have been recognized for their good thermal and long loop stability [16]. Importantly, the cobalt-free layered oxide cathode Li[Ni_xMn_y]O₂ has received much attention as one of the most promising materials for current LIBs. The greatest advantage of cobalt-free layered oxide cathodes is their ability to simultaneously meet the requirements of ultra-low cost and high energy density [17–19]. This has greatly driven the evolution of cathode materials from low-nickel to medium-nickel cobalt-free compositions.

In addition to the cobalt-free strategy, reducing the nickel content in Li[Ni_xMn_y]O₂ can further reduce the production costs of batteries. However, compared to high-nickel NCM cathodes, reducing the nickel content in Li[Ni_xMn_y]O₂ ($x, y > 0.2$) results in a lower effective energy density under the same charge/discharge voltage window [20,21]. To address this issue, Liu et al. [22] proposed that manganese substitution for cobalt in ternary cathode materials can be suitable for high-voltage operation. However, within the high-voltage electrochemical window (~4.5 V), the cathode material inevitably undergoes side reactions with the electrolyte, leading to severe structural degradation [23–25]. Simultaneously, the dissolution of transition metals is intensified during high-voltage charging, and transition metal impurities accumulate on the positive electrode through chemical reactions and degrade battery performance [26–30]. Zhang et al. [31] reported that tungsten coating is shown to decrease the median particle size and improve the cycling stability in half cells from 91% retained capacity after 100 cycles to 93% retained capacity when 0.3% tungsten is added. At 4.2 V, the NM64 material had a capacity of 161 mAh/g on the first charge, and at 4.4 V, there was 191 mAh/g on the first charge. Tang et al. [32] reported the full-cell over-metal deposition of NM64 at different voltages from 4.1 to 4.4 V and found that NM64 showed less over-metal deposition during cycling compared to other cathode materials, and they also demonstrated more excellent cycling performance.

Based on the above facts, the medium-nickel cobalt-free LiNi_{0.6}Mn_{0.4}O₂ (NM64) cathode offers the advantages of lower cost and higher energy density. In this paper, we systematically study the electrochemical performance of NM64 in different operating voltage ranges, including electrode energy density, initial efficiency, and reversible capacity after cycling. Through these analyses, we identified the optimal electrochemical operating voltage range for the NM64 cathode material, which achieves a balance between electrode energy density, initial efficiency, and reversible capacity. This approach fully utilizes the cost advantage, energy density advantage, and cycling stability of NM64, providing a feasible strategy for developing low-cost cathode materials for LIBs with high energy densities and excellent cycle stability levels.

2. Experimental Section

2.1. Material Preparation

Firstly, 2M NiSO₄·6H₂O and 2M MnSO₄·H₂O were mixed in a molar ratio (Ni:Mn) of 6:4. Meanwhile, 1M NH₃·H₂O and 4M NaOH were added into the reactor. The temperature of the reactor was maintained at 50 °C, with a stirring speed of 800 r/min. Additionally, the pH value was maintained within the range of 10 ± 0.3. The resulting precipitate was

washed, aged in deionized water, filtered, and dried in vacuum overnight at 120 °C to obtain the $\text{Ni}_{0.6}\text{Mn}_{0.4}(\text{OH})_2$ precursor. After that, $\text{Ni}_{0.6}\text{Mn}_{0.4}(\text{OH})_2$ was mixed and ground with $\text{LiOH}\cdot\text{H}_2\text{O}$ sufficiently, with the ratio of lithium and transition metal being 1.05, and calcined at 500 °C for 5 h and then 900 °C for 20 h in a pure oxygen atmosphere to obtain the $\text{LiNi}_{0.6}\text{Mn}_{0.4}\text{O}_2$ cathode material.

2.2. Analytical Techniques

$\text{K}\alpha$ -ray diffraction (XRD, Rigaku DMAX 2500, Tokyo, Japan) and (XPS Thermo Scientific, Escalab 250 XI, Waltham, MA, USA) were used to determine the structures of the samples and valence states of the elements, and the XRD was refined using GSAS software (GSAS-II). The morphologies of the samples were evaluated by scanning electron microscopy (SEM, Hitachi S-4800, Tokyo, Japan).

2.3. Electrochemical Measurements

Electrochemical performance was tested using a Coin C2016 battery. Mixed in NMP solvent were the cathode material (80 wt%), Super P (10 wt%), and polyvinylidene fluoride (10 wt%), which were then coated onto aluminum foil and dried in a vacuum oven at 100 °C for 6 h. The electrolyte consisted of 1 mol L⁻¹ LiPF₆ and an ethylene carbonate (EC)/dimethyl carbonate (DMC) (*v/v* = 1:1) mix. Subsequently, the coated foil was cut into disks of 13 mm diameter with 1.51–1.54 mg/cm² of active substance. The cells with lithium metal as the anode were placed in a dry glove box filled with Ar gas atmosphere. Constant current charge/discharge characteristics were measured using a Neware battery cycler (1 C = 180 mA/g).

3. Results and Discussion

3.1. Morphological and Structural Characterization

The specific material is analyzed as follows. Firstly, the process of synthesis for the preparation of NM64 cathode materials is shown in Figure 1a, including the schematic diagram of precursor synthesis and the schematic of secondary particles formed by high-temperature sintering in an oxygen atmosphere. In detail, the morphology of the NM64 precursor is shown in Figure 1b,c. Evidently, the secondary particles of the precursor are similar to woven balls with sizes of 3–4 μm , and they are formed by the stacking of fine needle-like primary particles. After high-temperature calcination, the secondary particles have a dense spheroidal shape, consisting of many small spherical primary particles of about 0.2 μm stacked together (Figure 1d,e), resulting in a particle size range of approximately 3–4 μm . In addition, SEM-EDS shows that the elements of Ni, Mn, and O are homogeneously distributed on the surfaces of secondary particles (Figure 1f).

Secondly, the crystal structure of NM64 is analyzed by X-ray diffraction (XRD). The XRD spectra (Figure 2a) and Rietveld refinement (Figure 2b) show that NM64 exhibits a hexagonal layered structure ($\alpha\text{-NaFeO}_2$ type, R-3m space group) with no impurity phases. Additionally, the splitting of the peaks (006)/(012) and (018)/(110) of the NM64 sample is obvious, which indicates the electrode material's high crystallinity and obvious layer structure [33,34]; the $I_{(003)}/I_{(104)}$ ratio of 1.384 (>1.2) indicates that the electrode material has a low degree of Li-Ni mixing and discharging [35–38]. Thirdly, based on the XPS test analysis, the content of Ni^{3+} in NM64 is 71.45%, and the smaller proportion of Ni^{2+} is conducive to reducing the cation mixing and stabilizing the electrode structure. The characteristic peak of Mn in the 3/2p orbital Mn^{3+} accounts for 47.41%, and the smaller amount of Mn^{3+} can effectively alleviate the Jahn-Teller effect, alleviating the transformation of the electrode material to the undesirable structure [39]. In addition, due to the fact that the ternary cathode material is extremely unstable in air, it is easy to react with moisture and CO_2 in the air, generating Li_2CO_3 and other residual lithium compounds on the surface of the material, so the characteristic peaks at the binding energy of O1s at 531.7 eV are the characteristic peaks of Li_2CO_3 [40], and the peak content of lattice oxygen at 528.9 eV can be seen as 28.36% of the characteristic peak at the binding energy.

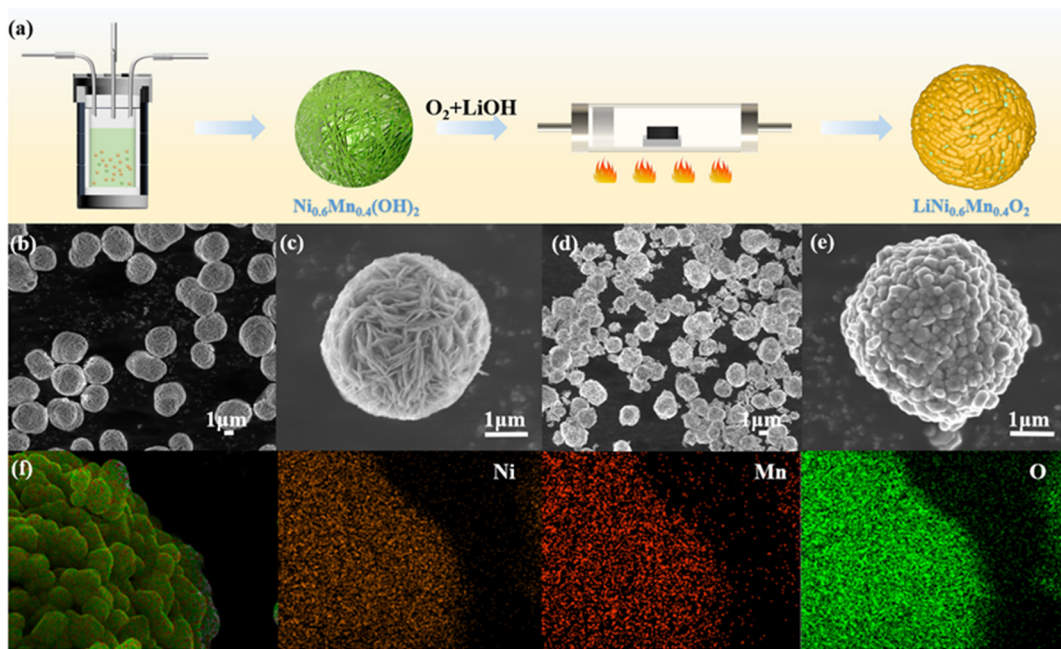


Figure 1. (a) Schematic diagram of the NM64 synthesis process. (b,c) Scanning electron microscope images of the NM64 precursor. (d,e) Scanning electron microscope images of NM64. (f) EDS mapping of NM64 elements.

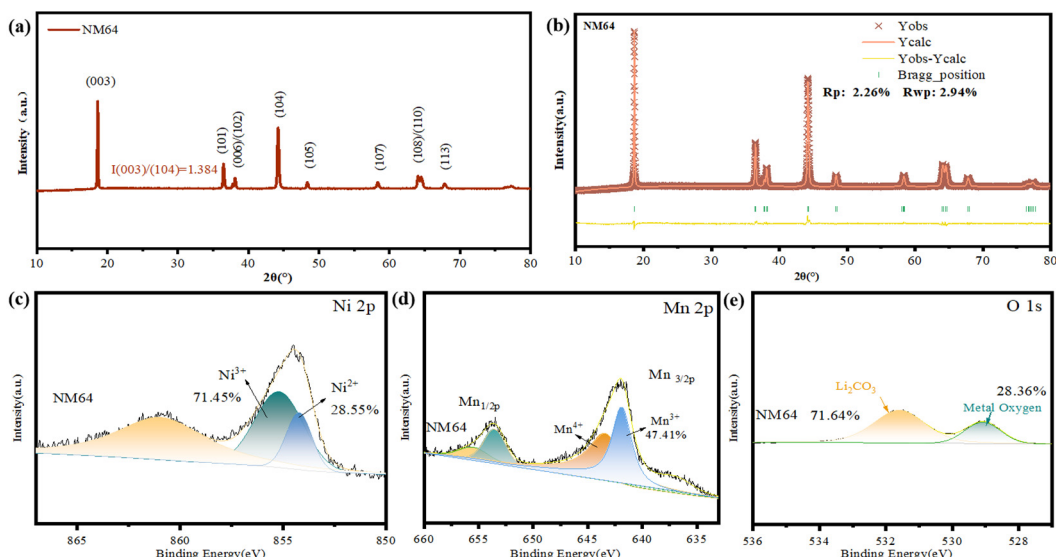


Figure 2. (a) XRD spectra and (b) Rietveld refinement maps of NM64. XPS spectra of NM64 (c) Ni 2p, (d) Mn 2p, and (e) O 1s.

3.2. Electrochemical Performance Analysis

The initial charge/discharge curves of NM64 at different voltages are shown in Figure 3a; the initial Coulombic Efficiencies at 4.2 V, 4.3 V, 4.4 V, 4.5 V, 4.6 V, and 4.7 V are 81.42%, 82.49%, 83.34%, 84.49%, 80.51%, and 74.65%, respectively. As the charging cut-off voltage increases, the initial Coulombic efficiency of NM64 exhibits a trend of initially increasing and then decreasing (Figure 3a). It is interesting to note that in the voltage range of 3.0–4.5 V, NM64 exhibits a remarkably high initial Coulombic efficiency, reaching up to 84.49%. The specific reason for this trend is that as the charging termination voltage is further increased, the initial Coulombic efficiency tends to gradually decrease, which is primarily due to the intensification of side reactions under high voltage conditions at

the electrode/electrolyte interface. Furthermore, the initial discharge specific capacities at 0.1 C (18 mA/g) current density are 133.96 mAh/g, 152.03 mAh/g, 172.45 mAh/g, 197.84 mAh/g, 209.38 mAh/g, and 213.95 mAh/g, respectively, and the initial discharge capacity showed an increase with the increase in the voltage interval trend. Figure 3b illustrates the capacity retention of NM64 during 50 cycles at a 1 C rate under different voltages. The results show that the capacity retention percentages at 4.2 V, 4.3 V, 4.4 V, 4.5 V, 4.6 V, and 4.7 V are 99.5%, 99.48%, 98.7%, 96%, 95.05%, and 95.02%, respectively. Contrary to the trend observed in the discharge capacity, the cycle retention rate of NM64 decreases as the voltage increases (Figure 3b). It is worth noting that the discharge specific capacitance improves with the increase in the charge termination voltage, and the capacity increases at both 0.1 C and 1 C current densities are the largest when the charging voltage is increased from 4.4 V to 4.5 V, being 25.39 mAh/g and 17.04 mAh/g, respectively (Figure 3c,d). In a word, on one hand, the electrode energy density of NM64 is not utilised repeatedly when the supply voltage is lower than 4.4 V. On the other hand, the electrode Coulombic efficiency and capacity retention rate of NM64 showed significant decreases when the charge termination voltage is higher than the 4.6 V, which indicates that the cycling stability levels of the electrodes decreased significantly. Taking into account factors such as electrode energy density, initial efficiency, and cycling reversible specific capacity, NM64 shows more excellent electrochemical performance in the operating voltage range of 4.4~4.6 V.

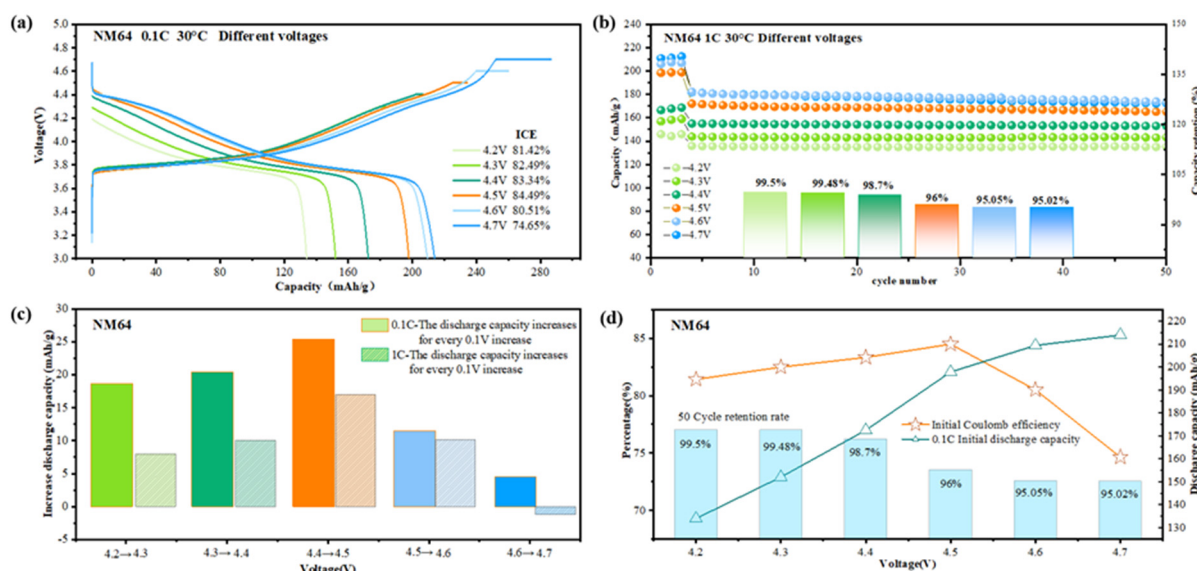


Figure 3. (a) The NM64 electrode under different voltage windows at the first charge/discharge curve with a current density of 0.1 C (18 mA/g). (b) The cycling performance of the NM64 electrode at 1 C magnification for 50 cycles under different voltage windows. (c) A histogram of capacity increase per 0.1 V rise in the NM64 charging voltage window at 0.1 C and 1 C current densities. (d) Comparison of performance metrics of NM64 electrodes in terms of first-time Coulombic efficiency, 0.1 C first lap discharge capacity, and 50-lap cycle retention at 1 C current density under different voltage windows.

For further research into the electrochemical performance of NM64 at 4.4~4.6 V, NM64 is tested for long-cycle stability at a 1 C current density. Initial discharge capacities of the NM64 material at 4.4 V, 4.5 V, and 4.6 V voltages are 155.12 mAh/g, 172 mAh/g, and 182.18 mAh/g. In contrast, although the retention rate decreases as the cut-off voltage increases, the sample under a 4.5 V turn-off voltage still retains a capacity close to 150 mAh/g (149.16 mAh/g) after 150 cycles, whereas the post-cycle capacities of the samples at 4.4 V and 4.6 V cut-off voltages were only 147.49 mAh/g and 142.21 mAh/g (Figure 4a), respectively. This indicates that the NM64 material achieves a balance between electrode energy density and structural stability at a 4.5 V cut-off voltage, resulting in excellent capacity retention. In addition, it can be seen from the charge/discharge curves under different

cycles (Figure 4b–d) that NM64 has a good discharge platform retention under high-voltage cycling. At the same time, the peak shapes of the dQ/dV curves after 150 cycles at 4.4 V and 4.5 V have good retention (Figure 4e–g), indicating that the NM64 material has excellent reversibility at 4.4 V and 4.5 V voltages. In addition, no significant second-phase M (monoclinic phase) appeared during the phase transition; this may be related to the absence of Co and the nature of the material [23]. It is noteworthy that the dQ/dV curves of NM64 in the 3.0–4.5 V and 3.0–4.6 V voltage window interval show a H2 \rightarrow H3 phase transition around 4.4 V (Figure 4f,g) and, in the deep-charged state, the anisotropic contraction/expansion of the lattice structure caused by the H2 \rightarrow H3 phase transition in the layered cathode. The mechanical stability of polycrystalline anode particles is undermined by the resulting structural stresses as microcrack nucleation releases locally accumulated stresses along grain boundaries, which allows the electrolyte to penetrate into the anode particles and damage their inner surfaces [41]. Ultimately, the reduction peak potentials of the 4.4 V, 4.5 V, and 4.6 V samples decreased by 0.096 V, 0.012 V, and 0.0136 V at around 4.1 V, respectively, indicating that the reversibility of the material weakens with the increasing voltage [42–44].

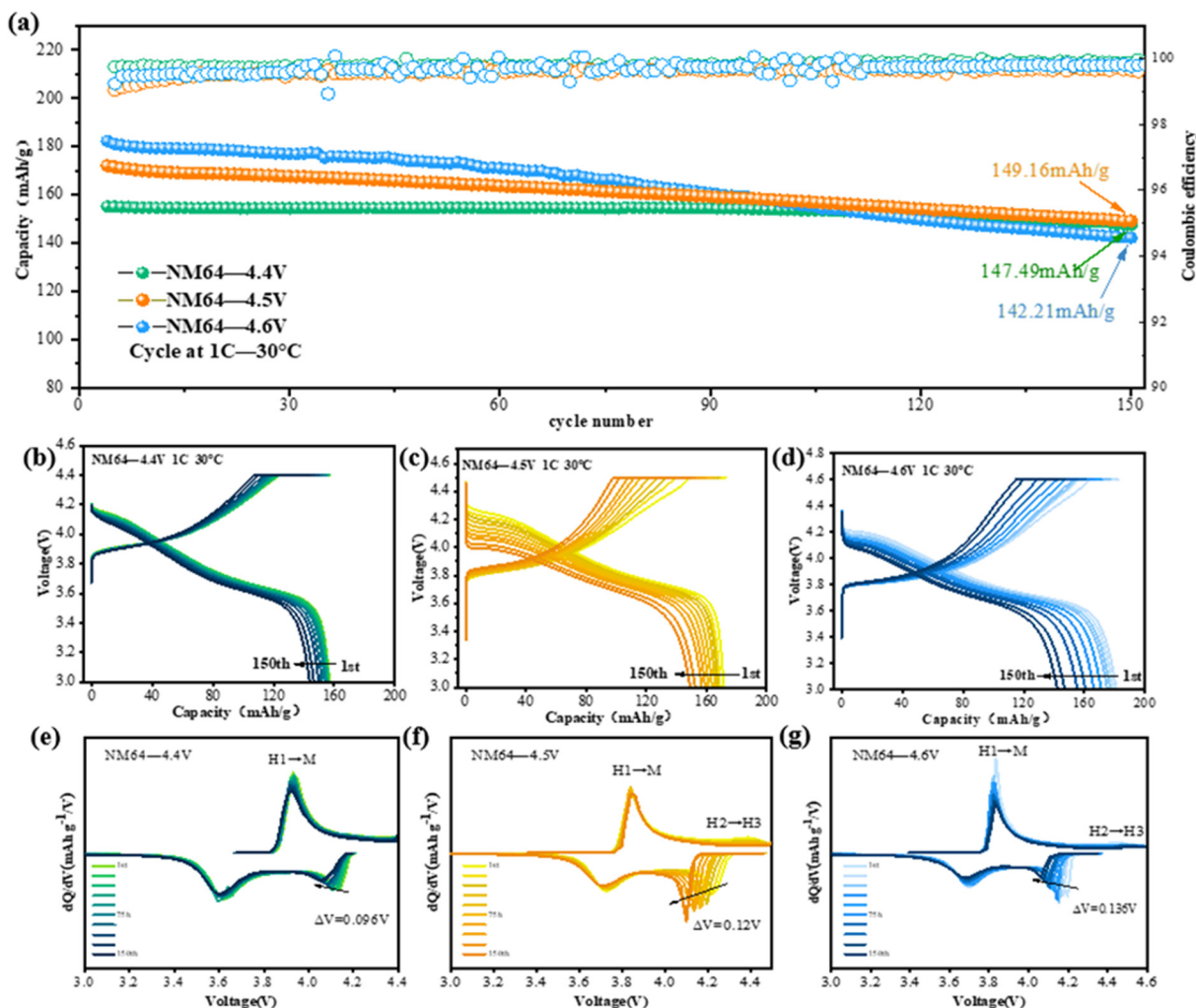


Figure 4. (a) Cycling performance of NM64 at 1 C (current density 180 mA/g) multiplicity in 3.0–4.4 V, 3.0–4.5 V, and 3.0–4.6 V voltage windows. (b) Charge/discharge curves of NM64-4.4 V, (c) NM64-4.5 V, and (d) NM64-4.6 V at 1 C. (e) Corresponding dQ/dV curves of NM64-4.4 V, (f) NM64-4.5 V, and (g) NM64-4.6 V during charging/discharging.

3.3. Post-Cycle Analysis

Figure 5a–c shows the SEM images of NM64 after 150 cycles at 1 C in 4.4 V, 4.5 V, and 4.6 V. It can be observed in Figure 5c that the secondary particle structure of NM64 is severely damaged at 4.6 V, which exacerbates the side reactions at the electrode/electrolyte interface, which leads to the dissolution of the transition metals and the collapse of the crystal structure [42]. In contrast, NM64 electrodes can maintain intact spherical particles satisfactorily at voltages of 4.4 V and 4.5 V (Figure 5a,b). The erosion of the electrolyte on the surface and in the interior of the material is effectively suppressed, and the secondary particles have better structural stability. Moreover, Figure 5d shows the XRD characterization result after 150 cycles at 4.4 V, 4.5 V, and 4.6 V. And the peaks of the material (003) at different voltages are shifted to the left to different extents after cycling for 150 cycles, and all of results display irreversible structural damages, though the topography still keeps the typical layered structure. More importantly, the intensity of the (003) peak decreases as the voltage increases, indicating a gradual weakening of the layered structure feature, while the (108)/(110) splitting peaks at 4.4 V and 4.5 V are obvious, indicating a better structural integrity [45,46]. Contrarily, the (108)/(110) splitting peaks are obviously weakened at 4.6 V, indicating that the material's structure has suffered from more serious irreversible damage at a voltage of more than 4.5 V.

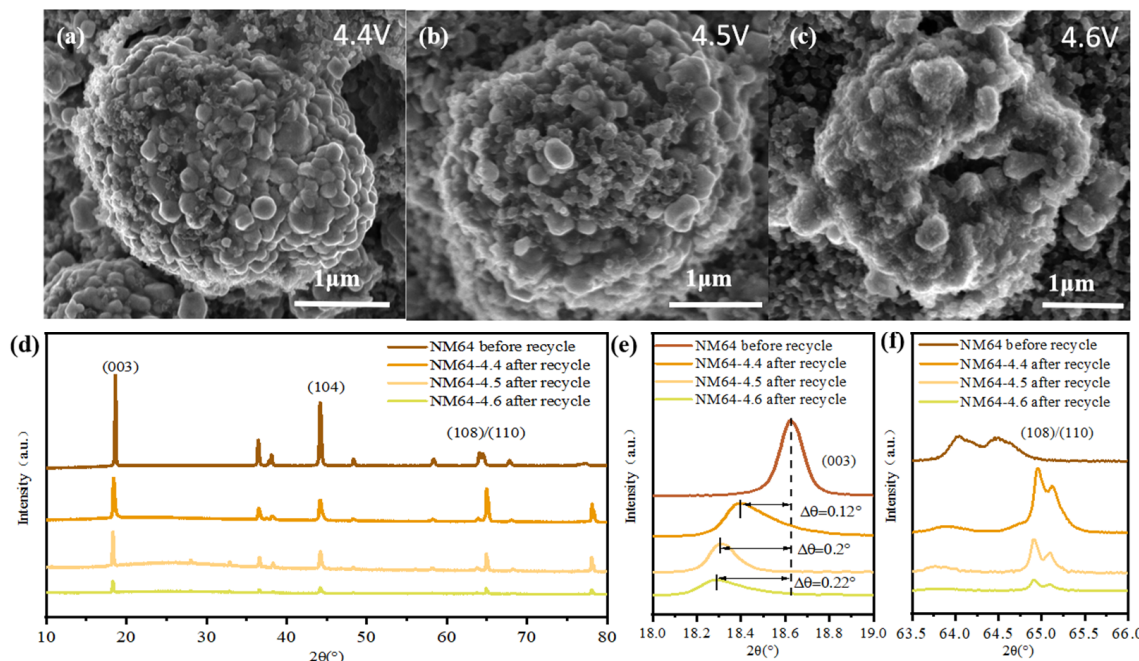


Figure 5. Scanning electron microscope images of (a) NM64-4.4 V, (b) NM64-4.5 V, and (c) NM64-4.6 V after 150 cycles. (d–f) XRD spectra of NM64 after 150 cycles compared with the pre-cycling XRD patterns and enlarged views of some diffraction peaks.

4. Conclusions

One effective strategy is to develop cobalt-free nickel-rich cathode materials to reduce battery costs and overcome the constraints of scarce cobalt resources. It is worth noting that nickel–manganese-rich $\text{LiNi}_{0.6}\text{Mn}_{0.4}\text{O}_2$ (NM64) offers the advantages of lower cost and higher energy density. This study focuses on investigating the electrochemical performance of NM64 within different voltage windows, specifically 4.2–4.7 V, and explores the optimal voltage range that provides a balance between structural stability and cycling performance. Primarily, the results show that NM64 exhibits excellent electrochemical performance within the voltage range of 3.0–4.5 V. At a current density of 0.1 C, NM64 achieves a reversible specific capacity of 197.84 mAh/g and an electrode energy density of 784.08 Wh/kg, with an impressive initial Coulombic efficiency of 84.49%. Increasing the

cut-off voltage from 4.4 V to 4.5 V leads to the maximum capacity enhancement at current densities of 0.1 C and 1 C, with increases of 25.39 mAh/g and 17.04 mAh/g, respectively. Moreover, even after 150 cycles at 1 C, NM64 retains a high reversible specific capacity of nearly 150 mAh/g, with a capacity retention rate of 86%, showcasing outstanding comprehensive electrochemical performance. Importantly, the morphological and structural characterization of NM64 after 150 cycles within the voltage range of 3.0–4.5 V reveals that the material maintains its intact morphology and exhibits no significant cracking. X-ray diffraction (XRD) analysis demonstrates the retention of the typical layered structure, indicating good structural stability. Based on these experimental findings, high-voltage NM64 in the 3.0–4.5 V range exhibits encouraging performance, providing new insights for high-voltage nickel–manganese-rich cathode materials for next-generation LIBs, with potential applications in future commercial batteries with high voltages and high energy densities.

Author Contributions: Y.Q. and Y.L. co-wrote this paper, to which S.H. and N.Q. contributed. Y.Q. and T.H. performed the experiments, to which J.G. and N.H. contributed. X.H., Y.L. and X.L. supervised this work. All authors have read and agreed to the published version of the manuscript.

Funding: This work was funded by the Shenzhen Science and Technology Program (JCYJ20230807112503008).

Data Availability Statement: The data that support the findings of this study are available from the corresponding authors upon reasonable request.

Acknowledgments: This work was financially supported by the Shenzhen Science and Technology Program.

Conflicts of Interest: The authors declare no conflict of interest.

References

- Wang, X.; Ding, Y.-L.; Deng, Y.-P.; Chen, Z. Ni-Rich/Co-Poor Layered Cathode for Automotive Li-Ion Batteries: Promises and Challenges. *Adv. Energy Mater.* **2020**, *10*, 1903864. [[CrossRef](#)]
- Li, H.; Cormier, M.; Zhang, N.; Inglis, J.; Li, J.; Dahn, J.R. Is Cobalt Needed in Ni-Rich Positive Electrode Materials for Lithium Ion Batteries? *J. Electrochem. Soc.* **2019**, *166*, A429. [[CrossRef](#)]
- Olivetti, E.A.; Ceder, G.; Gaustad, G.G.; Fu, X. Lithium-Ion Battery Supply Chain Considerations: Analysis of Potential Bottlenecks in Critical Metals. *Joule* **2017**, *1*, 229. [[CrossRef](#)]
- Shi, C.; Wang, T.; Liao, X.; Qie, B.; Yang, P.; Chen, M.; Wang, X.; Srinivasan, A.; Cheng, Q.; Ye, Q.; et al. Accordion-like stretchable Li-ion batteries with high energy density. *Energy Storage Mater.* **2019**, *17*, 136. [[CrossRef](#)]
- Bessette, S.; Paoella, A.; Kim, C.; Zhu, W.; Hovington, P.; Gauvin, R.; Zaghib, K. Nanoscale Lithium Quantification in $\text{Li}_x\text{Ni}_y\text{Co}_z\text{Mn}_w\text{O}_2$ as Cathode for Rechargeable Batteries. *Sci. Rep.* **2018**, *8*, 17575. [[CrossRef](#)] [[PubMed](#)]
- Zhang, J.-N.; Li, Q.; Ouyang, C.; Yu, X.; Ge, M.; Huang, X.; Hu, E.; Ma, C.; Li, S.; Xiao, R.; et al. Trace doping of multiple elements enables stable battery cycling of LiCoO_2 at 4.6 V. *Nat. Energy* **2019**, *4*, 594. [[CrossRef](#)]
- Tsai, P.-C.; Wen, B.; Wolfman, M.; Choe, M.-J.; Pan, M.S.; Su, L.; Thornton, K.; Cabana, J.; Chiang, Y.-M. Single-particle measurements of electrochemical kinetics in NMC and NCA cathodes for Li-ion batteries. *Energy Environ. Sci.* **2018**, *11*, 860. [[CrossRef](#)]
- Luo, Y.-h.; Wei, H.-x.; Tang, L.-b.; Huang, Y.-d.; Wang, Z.-y.; He, Z.-j.; Yan, C.; Mao, J.; Dai, K.; Zheng, J.-c. Nickel-rich and cobalt-free layered oxide cathode materials for lithium ion batteries. *Energy Storage Mater.* **2022**, *50*, 274. [[CrossRef](#)]
- Hu, E.; Yu, X.; Lin, R.; Bi, X.; Lu, J.; Bak, S.; Nam, K.-W.; Xin, H.L.; Jaye, C.; Fischer, D.A.; et al. Evolution of redox couples in Li- and Mn-rich cathode materials and mitigation of voltage fade by reducing oxygen release. *Nat. Energy* **2018**, *3*, 690. [[CrossRef](#)]
- Liu, T.; Dai, A.; Lu, J.; Yuan, Y.; Xiao, Y.; Yu, L.; Li, M.; Gim, J.; Ma, L.; Liu, J.; et al. Correlation between manganese dissolution and dynamic phase stability in spinel-based lithium-ion battery. *Nat. Commun.* **2019**, *10*, 4721. [[CrossRef](#)]
- Tong, H.; Yuan, X.; Qin, N.; Han, Y.; Cheng, Y.; Ji, F.; Tuo, R.; Liang, C.; Wang, Y.; Tong, Q.; et al. Plane-controlled growth strategy improves electrochemical performance of cobalt-free $\text{LiNi}_{0.9}\text{Mn}_{0.1}\text{O}_2$ cathode. *Prog. Nat. Sci.-Mater. Int.* **2024**, *34*, 569. [[CrossRef](#)]
- Yi, M.C.; Dolocan, A.; Manthiram, A. Stabilizing the Interphase in Cobalt-Free, Ultrahigh-Nickel Cathodes for Lithium-Ion Batteries. *Adv. Funct. Mater.* **2023**, *33*, 2213164. [[CrossRef](#)]
- Liu, X.J.; Chen, M.Y.; Ma, J.J.; Liang, J.Q.; Li, C.S.; Chen, C.J.; He, H.B. Advances in the synthesis strategies of carbon-based single-atom catalysts and their electrochemical applications. *China Powder Sci. Technol.* **2024**, *30*, 35.
- Yan, P.; Zheng, J.; Liu, J.; Wang, B.; Cheng, X.; Zhang, Y.; Sun, X.; Wang, C.; Zhang, J.-G. Tailoring grain boundary structures and chemistry of Ni-rich layered cathodes for enhanced cycle stability of lithium-ion batteries. *Nat. Energy* **2018**, *3*, 600. [[CrossRef](#)]

15. Mu, L.; Yang, Z.; Tao, L.; Waters, C.K.; Xu, Z.; Li, L.; Sainio, S.; Du, Y.; Xin, H.L.; Nordlund, D.; et al. The sensitive surface chemistry of Co-free, Ni-rich layered oxides: Identifying experimental conditions that influence characterisation results. *J. Mater. Chem. A* **2020**, *8*, 17487. [[CrossRef](#)]
16. Kaboli, S.; Demers, H.; Paoella, A.; Darwiche, A.; Dontigny, M.; Clément, D.; Guerfi, A.; Trudeau, M.L.; Goodenough, J.B.; Zaghib, K. Behaviour of Solid Electrolyte in Li-Polymer Battery with NMC Cathode via in-Situ Scanning Electron Microscopy. *Nano Lett.* **2020**, *20*, 1607. [[CrossRef](#)] [[PubMed](#)]
17. Hu, G.; Zhang, Y.; Zeng, J.; Fang, Z.; Cao, Y.; Peng, Z.; Tan, X.; Du, K. Mo-F Co-Doping $\text{LiNi}_{0.83}\text{Co}_{0.11}\text{Mn}_{0.06}\text{O}_2$ Stabilizes the Structure and Induces Compact Primary Particle To Improve the Electrochemical Performance. *ACS Appl. Energy Mater.* **2023**, *6*, 3834. [[CrossRef](#)]
18. Kim, Y.; Seong, W.M.; Manthiram, A. Cobalt-free, high-nickel layered oxide cathodes for lithium-ion batteries: Progress, challenges, and perspectives. *Energy Storage Mater.* **2021**, *34*, 250. [[CrossRef](#)]
19. Park, G.-T.; Namkoong, B.; Kim, S.-B.; Liu, J.; Yoon, C.S.; Sun, Y.-K. Introducing high-valence elements into cobalt-free layered cathodes for practical lithium-ion batteries. *Nat. Energy* **2022**, *7*, 946. [[CrossRef](#)]
20. Zhang, R.; Wang, C.; Zou, P.; Lin, R.; Ma, L.; Yin, L.; Li, T.; Xu, W.; Jia, H.; Li, Q.; et al. Compositionally complex doping for zero-strain zero-cobalt layered cathodes. *Nature* **2022**, *610*, 67. [[CrossRef](#)]
21. de Biasi, L.; Schwarz, B.; Brezesinski, T.; Hartmann, P.; Janek, J.; Ehrenberg, H. Chemical, Structural, and Electronic Aspects of Formation and Degradation Behaviour on Different Length Scales of Ni-Rich NCM and Li-Rich HE-NCM Cathode Materials in Li-Ion Batteries. *Adv. Mater.* **2019**, *31*, 1900985. [[CrossRef](#)] [[PubMed](#)]
22. Zhang, S.S. Problems and their origins of Ni-rich layered oxide cathode materials. *Energy Storage Mater.* **2020**, *24*, 247. [[CrossRef](#)]
23. Liu, T.; Yu, L.; Liu, J.; Lu, J.; Bi, X.; Dai, A.; Li, M.; Li, M.; Hu, Z.; Ma, L.; et al. Understanding Co roles towards developing Co-free Ni-rich cathodes for rechargeable batteries. *Nat. Energy* **2021**, *6*, 277. [[CrossRef](#)]
24. Fan, X.; Ou, X.; Zhao, W.; Liu, Y.; Zhang, B.; Zhang, J.; Zou, L.; Seidl, L.; Li, Y.; Hu, G.; et al. In situ inorganic conductive network formation in high-voltage single-crystal Ni-rich cathodes. *Nat. Commun.* **2021**, *12*, 5320. [[CrossRef](#)]
25. Jung, S.-K.; Gwon, H.; Hong, J.; Park, K.-Y.; Seo, D.-H.; Kim, H.; Hyun, J.; Yang, W.; Kang, K. Understanding the Degradation Mechanisms of $\text{LiNi}_{0.5}\text{Co}_{0.2}\text{Mn}_{0.3}\text{O}_2$ Cathode Material in Lithium Ion Batteries. *Adv. Energy Mater.* **2014**, *4*, 1300787. [[CrossRef](#)]
26. Fan, X.; Hu, G.; Zhang, B.; Ou, X.; Zhang, J.; Zhao, W.; Jia, H.; Zou, L.; Li, P.; Yang, Y. Crack-free single-crystalline Ni-rich layered NCM cathode enable superior cycling performance of lithium-ion batteries. *Nano Energy* **2020**, *70*, 104450. [[CrossRef](#)]
27. Betz, J.; Brinkmann, J.-P.; Nölle, R.; Lürenbaum, C.; Kolek, M.; Stan, M.C.; Winter, M.; Placke, T. Cross Talk between Transition Metal Cathode and Li Metal Anode: Unravelling Its Influence on the Deposition/ Dissolution Behaviour and Morphology of Lithium. *Adv. Energy Mater.* **2019**, *9*, 1900574. [[CrossRef](#)]
28. Liu, W.; Li, J.; Li, W.; Xu, H.; Zhang, C.; Qiu, X. Inhibition of transition metals dissolution in cobalt-free cathode with ultrathin robust interphase in concentrated electrolyte. *Nat. Commun.* **2020**, *11*, 3629. [[CrossRef](#)]
29. Li, Y.; Li, W.; Shimizu, R.; Cheng, D.; Nguyen, H.; Paulsen, J.; Kumakura, S.; Zhang, M.; Meng, Y.S. Elucidating the Effect of Borate Additive in High-Voltage Electrolyte for Li-Rich Layered Oxide Materials. *Adv. Energy Mater.* **2022**, *12*, 2103033. [[CrossRef](#)]
30. Deng, F.; Wang, Y.L.; Zhang, Y.F.; Li, J.X.; Guan, R.; Li, K.Q.; Su, J.Z.; Sun, H.R.; Han, H.L.; Yuan, Z.G.; et al. Prepared of porous magnesium oxide crystal with hydromagnesite method. *China Powder Sci. Technol.* **2024**, *30*, 138.
31. Tang, B.; Zhang, N.; Alter, E.; Eldesoky, A.; Dahn, J.R. Transition Metal Dissolution from Single Crystal $\text{Li}[\text{Ni}_{1-x-y}\text{Mn}_x\text{Co}_y]\text{O}_2$ and $\text{Li}[\text{Ni}_{1-x}\text{Mn}_x]\text{O}_2$ Positive Electrodes Subjected to Aggressive Conditions. *J. Electrochem. Soc.* **2024**, *171*, 010518.
32. Garayt, M.D.L.; Zhang, N.; Yu, S.; Abraham, J.J.; Murphy, A.; Omessi, R.; Ye, Z.; Azam, S.; Johnson, M.B.; Yang, C.; et al. Single Crystal $\text{Li}_{1+x}[\text{Ni}_{0.6}\text{Mn}_{0.4}]_{1-x}\text{O}_2$ Made by All-Dry Synthesis. *J. Electrochem. Soc.* **2023**, *170*, 060529. [[CrossRef](#)]
33. Zhang, X.; Cui, Z.; Manthiram, A. Insights into the Crossover Effects in Cells with High-Nickel Layered Oxide Cathodes and Silicon/Graphite Composite Anodes. *Adv. Energy Mater.* **2022**, *12*, 2103611. [[CrossRef](#)]
34. Zhao, W.; Zou, L.; Zhang, L.; Fan, X.; Zhang, H.; Pagani, F.; Brack, E.; Seidl, L.; Ou, X.; Egorov, K.; et al. Assessing Long-Term Cycling Stability of Single-Crystal Versus Polycrystalline Nickel-Rich NCM in Pouch Cells with 6 mAh cm^{-2} Electrodes. *Small* **2022**, *18*, 2107357.
35. Wang, B.; Zhang, F.-l.; Zhou, X.-a.; Wang, P.; Wang, J.; Ding, H.; Dong, H.; Liang, W.-B.; Zhang, N.-S.; Li, S.-Y. Which of the nickel-rich NCM and NCA is structurally superior as a cathode material for lithium-ion batteries? *J. Mater. Chem. A* **2021**, *9*, 13540. [[CrossRef](#)]
36. Wu, H.E.; Fei, G.T.; Gao, X.D.; Guo, X.; Gong, X.X.; Ma, X.L.; Wang, Q.; Xu, S.H. Research progress on preparation and application of polyaniline and its composite materials. *China Powder Sci. Technol.* **2023**, *29*, 70.
37. Li, L.; Fu, L.; Li, M.; Wang, C.; Zhao, Z.; Xie, S.; Lin, H.; Wu, X.; Liu, H.; Zhang, L.; et al. B-doped and $\text{La}_4\text{NiLiO}_8$ -coated Ni-rich cathode with enhanced structural and interfacial stability for lithium-ion batteries. *J. Energy Chem.* **2022**, *71*, 588. [[CrossRef](#)]
38. Ji, Y.Q.; Yu, Z.H.; Yan, L.G.; Song, W. Research progress in preparation, modification and application of biomass-based single-atom catalysts. *China Powder Sci. Technol.* **2023**, *29*, 100.
39. Zhu, X.; Meng, F.; Zhang, Q.; Xue, L.; Zhu, H.; Lan, S.; Liu, Q.; Zhao, J.; Zhuang, Y.; Guo, Q.; et al. LiMnO_2 cathode stabilised by interfacial orbital ordering for sustainable lithium-ion batteries. *Nat. Sustain.* **2021**, *4*, 392. [[CrossRef](#)]
40. Hou, P.; Zhang, H.; Deng, X.; Xu, X.; Zhang, L. Stabilising the Electrode/Electrolyte Interface of $\text{LiNi}_{0.8}\text{Co}_{0.15}\text{Al}_{0.05}\text{O}_2$ through Tailoring Aluminum Distribution in Microspheres as Long-Life, High-Rate, and Safe Cathode for Lithium-Ion Batteries. *ACS Appl. Mater. Interfaces* **2017**, *9*, 29643. [[CrossRef](#)]

41. Ryu, H.-H.; Namkoong, B.; Kim, J.-H.; Belharouak, I.; Yoon, C.S.; Sun, Y.-K. Capacity Fading Mechanisms in Ni-Rich Single-Crystal NCM Cathodes. *ACS Energy Lett.* **2021**, *6*, 2726. [[CrossRef](#)]
42. Hu, D.; Su, Y.; Chen, L.; Li, N.; Bao, L.; Lu, Y.; Zhang, Q.; Wang, J.; Chen, S.; Wu, F. The mechanism of side reaction induced capacity fading of Ni-rich cathode materials for lithium ion batteries. *J. Energy Chem.* **2021**, *58*, 1. [[CrossRef](#)]
43. Yang, J.P.; Zhang, F.Z.; Chen, J. Structural design and application of fiber-based electrocatalytic materials. *China Powder Sci. Technol.* **2024**, *30*, 161.
44. Chen, S.; Qi, G.; Yin, R.; Liu, Q.; Feng, L.; Feng, X.; Hu, G.; Luo, J.; Liu, X.; Liu, W. Electrocatalytic nitrate-to-ammonia conversion on CoO/CuO nanoarrays using Zn-nitrate batteries. *Nanoscale* **2023**, *15*, 19577. [[CrossRef](#)]
45. Lu, G.; Meng, G.; Liu, Q.; Feng, L.; Luo, J.; Liu, X.; Luo, Y.; Chu, P.K. Advanced strategies for solid electrolyte interface design with MOF materials. *Adv. Powder Mater.* **2024**, *3*, 100154. [[CrossRef](#)]
46. Qin, D.D.; Ding, J.Y.; Linag, C.; Liu, Q.; Feng, L.G.; Luo, Y.; Hu, G.Z.; Luo, J.; Liu, X.J. Addressing Challenges and Enhancing Performance of Manganese-based Cathode Materials in Aqueous Zinc-Ion Batteries. *Acta Phys.-Chim. Sin.* **2024**, *40*, 2310034. [[CrossRef](#)]

Disclaimer/Publisher's Note: The statements, opinions and data contained in all publications are solely those of the individual author(s) and contributor(s) and not of MDPI and/or the editor(s). MDPI and/or the editor(s) disclaim responsibility for any injury to people or property resulting from any ideas, methods, instructions or products referred to in the content.